Soft Viscoelastic Magnetic Hydrogels from the *In Situ* Mineralization of Iron Oxide in Metal-Coordinate Polymer Networks

Jake Song, Sungjin Kim, Olivia Saouaf, Crystal Owens, Gareth H. McKinley,* and Niels Holten-Andersen*

Read Online

ACCESS | Metrics & More | Article Recommendations | Supporting Information

ABSTRACT: The design of soft magnetic hydrogels with high concentrations of magnetic particles is complicated by weak retention of the iron oxide particles in the hydrogel scaffold. Here, we propose a design strategy that circumvents this problem through the *in situ* mineralization of iron oxide nanoparticles within polymer hydrogels functionalized with strongly iron-coordinating nitrocatechol groups. The mineralization process facilitates the synthesis of a high concentration of large iron oxide nanoparticles (up to 57 wt % dry mass per single cycle) in a simple one-step process under ambient conditions. The resulting hydrogels are soft (kPa range) and viscoelastic and exhibit strong magnetic actuation. This strategy offers a pathway for the energy-efficient design of soft, mechanically robust, and magneto-responsive hydrogels for biomedical applications.

In situ Fe_3O_4 mineralized viscoelastic magnetic hydrogel

KEYWORDS: *metal-coordination, mineralization, hydrogel actuation, viscoelastic, smart biomaterials, magnetic hydrogels*
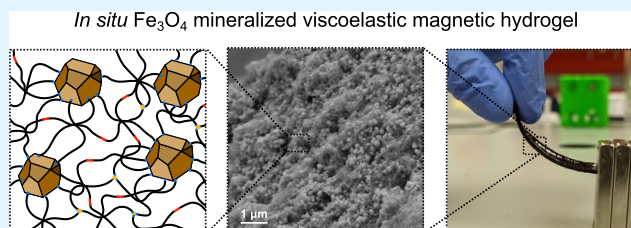
1. INTRODUCTION

Magneto-responsive soft materials have proven essential for the design of soft robots with programmable shape transformations,[1] biomimetic locomotion,[2,3] and biomedical function.[4] Such magnetic soft materials are usually designed by the embedding of iron oxide particles into a densely cross-linked polymer matrix such that the particles are stabilized in the polymer matrix through steric interactions. As the pore size of the matrix must not exceed the size of the magnetic particles, these design motifs typically allow the design of relatively stiff elastomeric materials in the MPa-GPa range.[5]

The design of softer magneto-responsive materials in the kPa range (wherein lie most tissues and cells in the body[6]) is desirable, particularly from a biomedical standpoint, as cell–biomaterial interactions are critically mediated by the mechanical properties of the biomaterial—for instance, a stiffness mismatch between biomaterials and cells is a known trigger of inflammatory responses.[7] Another important aspect of biomaterial design is the ability to undergo viscoelastic relaxation, which can facilitate cell proliferation within the matrix[8] and shape conformation of the material around tissues.[9] While softer magnetic hydrogels can be designed by grafting the iron oxide particles with covalently cross-linkable motifs,[10,11] this approach results in permanent networks with no stress relaxation ability, thus losing the functional advantages of viscoelasticity.

A softer viscoelastic magnetic hydrogel requires the use of noncovalent cross-linking motifs between the polymer and the particles. The majority of these approaches utilize biopolymers such as alginate, gelatin, and chitosan with relatively weak organic–inorganic interactions arising from carboxyl, amine, or simple steric interactions,[12–14] which results in a dynamic network but one in which the embedded particles are not tightly bound and can eventually diffuse out of the network. Thus, there is a need for designing magnetic hydrogel materials with strong chemical coupling between the iron oxide particles and the polymer matrix.

A promising solution for this problem is the use of metal-coordination interactions—particularly through the use of catechol ligands, which can bind strongly to transition metal species such as iron and titanium with near-covalent strength and yet reform spontaneously following breakage.[15–17] Prior works have demonstrated that these binding motifs can be used to design hydrogels with embedded iron oxide nanoparticles which are stable,[18,19] yet viscoelastic—with a slow stretched-exponential stress relaxation behavior that mimics those of tissues.[20] Despite these promising traits, these gels require the addition of precisely synthesized iron oxide nanoparticles with a large concentration of stabilizing polymers, which precludes the design of bulk-scale materials with a high density of magnetic particles. An alternative design
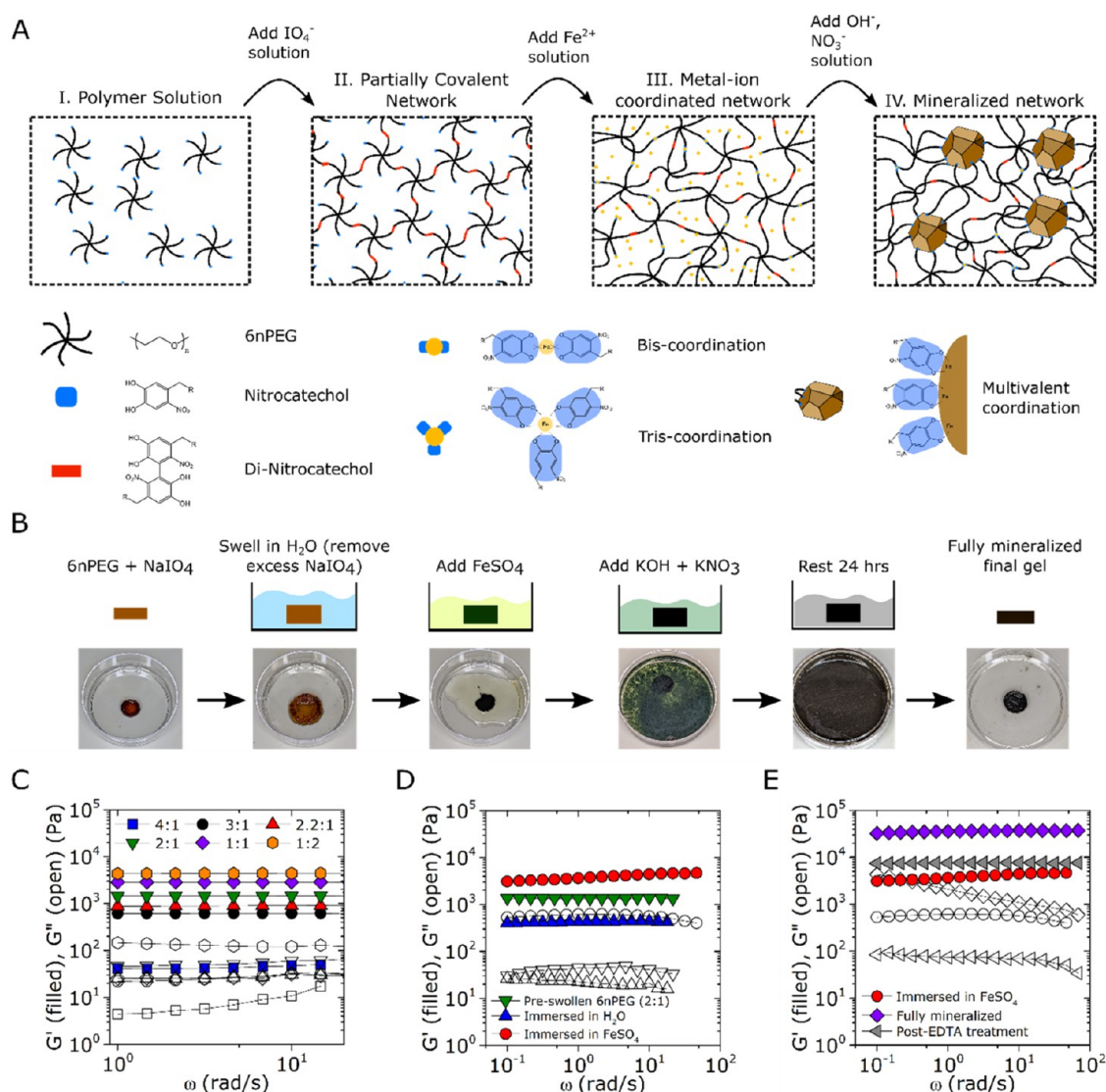
Figure 1. Illustration of method and mechanical characterization of the 6nPEG network during the mineralization process. (A) Schematic illustration of the mineralization strategy. (B) Visual illustration of the mineralization strategy. The 6nPEG hydrogel is formed by mixing with NaIO$_4$ in a 2:1 ligand-to-NaIO$_4$ ratio, which is then swollen in water overnight to remove excess NaIO$_4$. A 1 M solution of FeSO$_4$ is added to the gel sample and left for 3 h. KOH and KNO$_3$ are added to the FeSO$_4$-gel mixture and left for 24 h. The fully mineralized final gel is extracted and immersed in water for 2 h to remove poorly adsorbed Fe$_3$O$_4$ particles. (C) Frequency sweep of 6nPEG and NaIO$_4$ hydrogels at varying ligand-to-NaIO$_4$ ratios. (D) Frequency sweep of pre-swollen 6nPEG hydrogels, post-swollen 6nPEG hydrogels, and FeSO$_4$-immersed 6nPEG hydrogels. (E) Frequency sweep of FeSO$_4$-immersed 6nPEG hydrogels, fully mineralized hydrogels, and fully mineralized hydrogels after EDTA treatment. Data collected at the inertial limit of the rheometer (at a high angular frequency ω) are truncated for all measurements shown.

motif is to directly mineralize iron oxide nanoparticles within metal-coordinate polymer networks *in situ*.[21] While this approach is successful in creating viscoelastic metal-coordinate hydrogels with iron oxide nanoparticles, the approach requires the dropwise addition of reagents to a metal-ion coordinated network, which makes it difficult to mineralize a high concentration of iron oxides within the network and fabricate the hydrogel into desirable shapes.

Here, we propose a design strategy that allows for the mineralization of a high concentration of iron oxide nanoparticles in metal-coordinate polymer hydrogels *in situ*. We show that this can be achieved by a continuous mineralization of the polymer network using a solution bath and show that the polymer network can be stabilized from dissolution in the bath by the partial oxidative cross-linking of the polymer network. We show that the resulting hydrogel is soft (in the

kPa range), viscoelastic and can contain over 57 wt % dry mass of iron oxides in the network for a single mineralization cycle, which facilitates a strong magneto-responsive actuation response in the hydrogel. This design strategy thus offers the potential for designing soft viscoelastic magneto-responsive hydrogels for biomedical applications.

2. RESULTS AND DISCUSSION

2.1. Experimental Approach. Our model system is a network of 6-arm PEG stars functionalized with nitrocatechol (6nPEG), which is resistant to auto-oxidation[22] and thus serves as a better model system to study mineralization than the catechol-functionalized polymers.[21] We first sought to perform partial cross-linking of 6nPEG with covalent bonds such that the polymer network could sustain immersion in a solution bath and still retain enough nitrocatechol ligands for
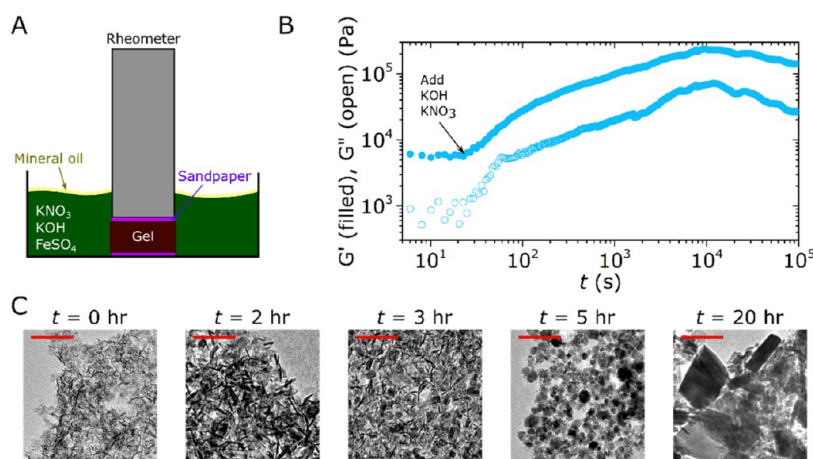
Figure 2. Temporal characterization of the nucleation and growth of Fe_3O_4 during partial oxidation. (A) Schematic illustration of the protocol used to monitor the nucleation and growth kinetics of Fe_3O_4 in the 6nPEG hydrogel. (B) Storage and loss moduli of the 6nPEG hydrogel measured during mineralization ($\omega = 10$ rad/s). (C) TEM images of the partial oxidation reaction conducted in a dilute solution (without the polymer matrix). Plate-like $Fe(OH)_2$ structures are observed immediately after the beginning of the reaction, followed by a gradual formation of more cubic Fe_3O_4 structures after 2 h. Scale bar = 100 nm.

metal-coordination (Scheme II, Figure 1A). Percolation study of 6nPEG with different concentrations of $NaIO_4$ shows that 6nPEG forms a loosely percolated network at a ligand-to-$NaIO_4$ ratio of 4:1 and becomes increasingly stiffer with a higher concentration of $NaIO_4$ (Figure 1C), in agreement with previous oxidation characterization of nitrocatechol.[23] While the 4:1 system would theoretically provide the highest nitrocatechol availability for metal-coordination, we found that loosely cross-linked networks such as the 4:1 and 3:1 systems did not maintain their shape upon swelling in water. We thus used a ligand-to-$NaIO_4$ ratio of 2:1 to design our model scaffolds; overnight water immersion of this partially covalent gel results in a modest drop in the elastic modulus but still allows the gel to retain its shape (Figure 1B,D). This model system was used for subsequent *in situ* mineralization of the Fe_3O_4 nanoparticles.

Our prior study performed *in situ* mineralization of Fe_3O_4 in the catechol-functionalized networks through a coprecipitation approach by simultaneous addition of Fe^{2+}, Fe^{3+}, and OH^- ions.[21] This results in the fast nucleation of Fe_3O_4 nanoparticles, which consequently impacts particle growth and results in the formation of mostly small particles.[24] The majority of the particles formed in our catechol-functionalized networks through coprecipitation were <10 nm in diameter, with the occasional presence of larger aggregates of <50 nm.[21] We thus sought to grow larger iron oxide nanoparticles in this study, which is possible through a different approach of forming Fe_3O_4—namely, via the partial oxidation approach[25−28]

$$Fe^{2+} + 2OH^- \rightarrow Fe(OH)_2$$

$$3Fe(OH)_2 + NO_3^- \rightarrow Fe_3O_4 + 4H_2O + NO_2^- \quad (1)$$
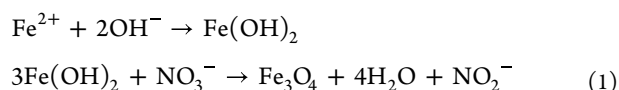
In this approach, the Fe^{2+} ions first precipitate and form rust crystals, which are shaped as hexagonal plates, and subsequent oxidation via nitrate ions facilitates the nucleation and growth of Fe_3O_4 nanoparticles. This approach results in the formation of much larger particles of Fe_3O_4 compared to the coprecipitation approach (as large as 1 μm in some reported cases[27]) because the nucleation rate of Fe_3O_4 is restricted by the rate at which the rust crystals are oxidized by the nitrate

ions, thus allowing the continued growth of the Fe_3O_4 particles.[29]

To perform partial oxidation mineralization of Fe_3O_4, we immerse the partially covalent swollen gel in a 1 M solution of $FeSO_4$, which preloads the covalent gel with a high concentration of Fe^{2+} ions. As the system is highly supersaturated, the nucleation and growth of Fe_3O_4 in our system is expected to occur throughout the entire matrix. The $FeSO_4$ solution has a pH of approximately 3.7, corresponding to a regime where nitrocatechol is partially deprotonated and undergoes *bis*-coordination bonding with Fe ions.[30] This results in a significant contraction of the gel and an increase in the modulus (Figure 1D); we interpret this as the gel having reached the point of full ligand saturation by the Fe^{2+} ions (Scheme III, Figure 1A). To this solution containing the solid gel and the $FeSO_4$ solution, we then added a mixture of KNO_3 and KOH to produce a final solution at a pH of 11.5. This results in the immediate formation of green precipitates of $Fe(OH)_2$ called "green rust",[27] and leaving this solution overnight results in the formation of black precipitates of Fe_3O_4 (Figure 1B).

The gel that has been mineralized in this manner exhibits a dramatic increase in the viscoelastic moduli compared to the gel swollen in $FeSO_4$ (Figure 1E). The resulting gel has a modulus of ~40 kPa, which is a modulus comparable to soft biological tissues such as the breast, heart, muscle, and intestine[31,32] and would make the gel appropriate for applications that interface with such systems. The gel is also viscoelastic, which is especially evident by the increasing loss modulus $G''(\omega)$ with decreasing frequency. This trend in G'' indicates the presence of an accessible relaxation mode at low frequencies. Given that the relaxation of the polymer-bridged Fe_3O_4–Fe_3O_4 interaction is slow and typically not accessible at these frequencies,[18,19,33] we hypothesized that this might be attributed to the presence of *tris*-coordination bonding between Fe ions and nitrocatechol. Evidence that the more kinetically stable *tris*-coordination bonding is occurring in the mineralized gels (rather than the more labile *bis*-coordination bonding) is exhibited by the differences in the viscoelastic properties of the gels; whereas the $FeSO_4$-immersed gels show a plateau in $G''(\omega)$ at a frequency range of $10^0 \leq \omega \leq 10^1$, the

mineralized gels show values of $G''(\omega)$ that continues to increase with decreasing frequency across the entire frequency range. To verify this, we immersed the resulting mineralized gel into ethylenediaminetetraacetic acid (EDTA) for 72 h; this solution can chelate the Fe^{2+} ions in the hydrogel and disrupt nitrocatechol-Fe^{2+} cross-linking but not the nitrocatechol-Fe_3O_4 cross-linking.[34] We find that the storage modulus of the mineralized gel decreases and the loss modulus $G''(\omega)$ disappears as well, instead becoming flat (Figure 1E). These results indicate that the final mineralized gel is a triple network consisting of covalent junctions, tris-coordinated metal-ion junctions, and nanoparticle-coordinated multivalent junctions (Scheme IV, Figure 1A).

2.2. Mineralization Kinetics. To develop a better understanding of the kinetics of particle self-assembly, we performed *in situ* rheological characterization of the gel during the mineralization process. Partially covalent hydrogels are soaked in $FeSO_4$ and transferred to a rheometer on a Petri dish, and a time-series measurement of the storage modulus $G'(\omega,t)$ and loss modulus $G''(\omega,t)$ at $\omega = 10$ rad/s is made, during which, a solution of KNO_3 and KOH is added to the Petri dish and the reactants are finally sealed with mineral oil (Figure 2A). This method provides qualitatively useful information on the temporal evolution of the mechanical properties of the gel, but bears some limitations as the diffusion of the reagents is confined to the narrow gap between the top plate of the rheometer geometry and the bottom of the Petri dish (thus causing a gradient in the extent of mineralization in the gel material). The addition of KNO_3 and KOH results in the immediate increase in the viscoelastic moduli of the hydrogels, lasting approximately 3 h before the modulus begins to decrease again (Figure 2B). To understand the microscopic origins of this behavior, we performed Reaction 1 in dilute solution (in the absence of the metal-coordinating polymer) and monitored its temporal evolution via TEM (Figure 2C). Consistent with prior observations,[29] we observe an immediate formation of plate-like structures, which are attributed to $Fe(OH)_2$ at $t = 0$ h, followed by a gradual formation of round or cubic structures that are attributed to Fe_3O_4 at $t = 2-3$ h, which eventually dominates the composition of the solution with time.

While the slow decrease in $G'(\omega)$ with the formation of Fe_3O_4 NPs is not fully understood, we believe there are two possible explanations for this effect. The first and more likely explanation is that at high pH, the nitrocatechol can "etch" the ions from the surface of Fe_3O_4 NPs due to the strong interactions with the Fe^{3+} sites on the surface.[35] This has been reported in previous studies, which show that at high pH, nitrocatechol-PEG networks with imbedded Fe_3O_4 NPs are crosslinked by both ion and nanoparticle-coordinated complexes.[19,34] The etching process results in fewer adherent polymers on the particle surface, resulting in a decrease in the modulus. The second explanation is that the nucleation and growth process of Fe_3O_4 results in significant internal stress in the network; internal stresses are a known presence in composite hydrogels[20] and can increase the modulus of a network,[36] and thus, internal stress relaxations can result in such a decrease in the modulus.

2.3. Mechanical Characterizations. Next, we performed mineralization reactions to obtain different volume fractions ϕ of the grown minerals to understand the mechanical reinforcement arising from the mineralization process. The volume fraction ϕ is determined by performing thermogravi-

metric analysis (TGA) of the gels and noting the sample mass at $T = 25\ °C$ (fully hydrated hydrogel), $T = 250\ °C$ (polymer and inorganic material), and $T = 550\ °C$ (inorganic material only) (Figure 3A). For the fully mineralized gel, we find a
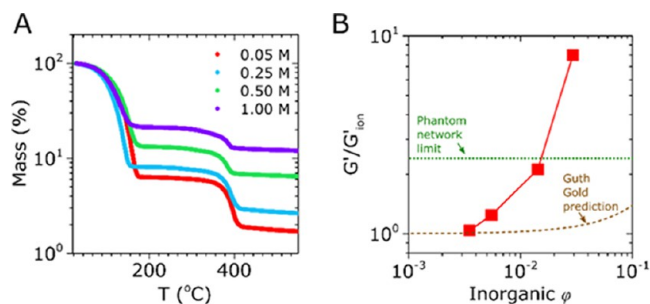
Figure 3. Concentration-dependent modulus of the mineralized 6nPEG gels. (A) TGA analysis of the 6nPEG gels that have been mineralized with varying concentrations of $FeSO_4$. (B) Storage modulus G' of the mineralized gels (normalized by the G'_{ion}, modulus of the $FeSO_4$-immersed system in Figure 1D) as a function of ϕ. The Guth-Gold predictions and maximum modulus values predicted from phantom network theory are also shown.

water/polymer/inorganic mass ratio of 79:9:12. Assuming that the inorganic contents are Fe_3O_4 ($\rho = 5.17$ g/cm^3), this suggests that the fully mineralized gel exhibits an inorganic volume fraction of $\phi = 3\%$ in the wet state, exceeding the yield in the prior study by 10-fold.[21] This also suggests that the mineralized particles account for 57 wt % of the dry mass (or 21.1% dry volume). We expect that repeated cycles may further increase the mineral density in the network, as shown in prior works.[12]

To obtain gels of different ϕ, we systematically lower the concentration of $FeSO_4$ used for making the mineralized gels (the amount of KOH mixture is controlled independently to ensure that the final pH of the gel is consistent around $\sim$11.5). In Figure 3B, we compare the storage modulus values of the mineralized gels with the storage modulus of the maximally metal-ion coordinated gel state (Scheme II, in Figure 1A), which was approximately 5 kPa as shown in Figure 1D. We find a systematic increase in the storage modulus of the mineralized gel with increasing inorganic ϕ, up to an 8-fold increase in the storage modulus compared to the maximally metal-ion coordinated state. The increase in G' is higher than what is possible via phantom network theory, which is used to predict an increase in the elastic modulus with increasing junction functionality.[37] If we assume that the 5 kPa modulus of the maximally metal-ion-coordinated state arises from a combination of two junctions, then the phantom network would predict that the resulting modulus is $G' = Fvk_BT$, where v is the density of the cross-links and $F = (1 - 1/f_1 - 1/f_2)$ is the junction-functionality-dependent scaling term.[38] Note that $G' = vk_BT$ is the affine prediction and thus F rescales the affine prediction based on the junction functionality in the network. With $f_1 = 6$ from the 6nPEG and $f_2 = 2$ from the bis-coordination or covalent cross-linking, the scaling term $F = 2:6$. Even if $f_2 = \infty$ as a result of the large iron oxide junctions, $F = 5:6$, which would represent a 2.5 fold increase in the modulus, and is therefore not sufficient to explain the 8-fold increase in the modulus observed in Figure 3B. Similarly, the Guth-Gold model—which estimates the increase in modulus of rubbers with the addition of filler via the relation $G'/G'_0 = 1 + 2.5\phi + 14.1\phi^2$—underpredicts the modulus increase in the
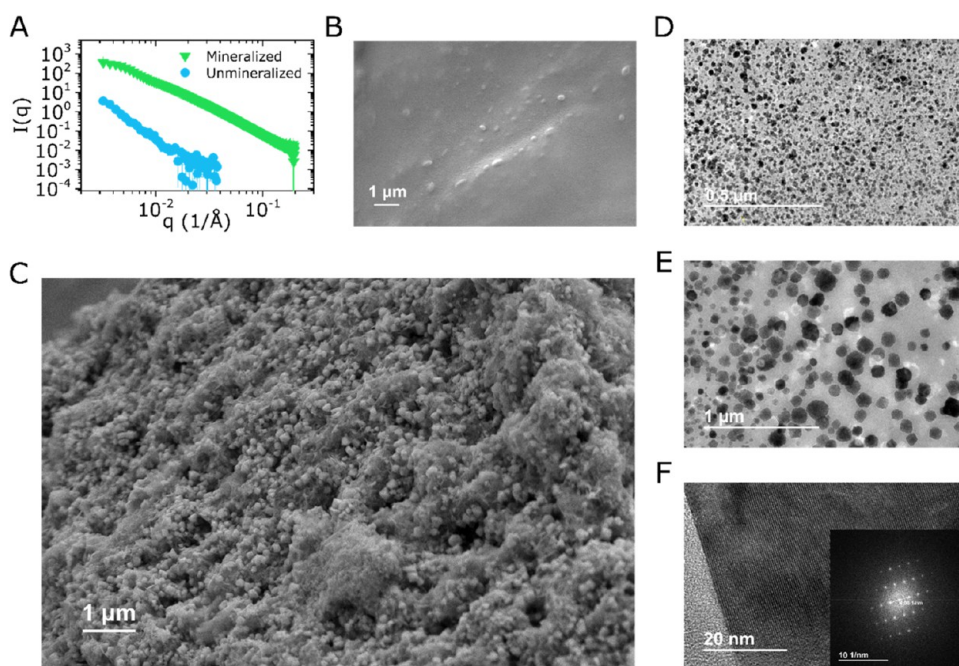
Figure 4. Structural characterization of the mineralized 6nPEG gels. (A) SAXS characterization of the 6nPEG network and the fully mineralized gel (first and last panels of Figure 1B). The plot shows the scattered intensity $I(q)$ of the materials plotted as a function of the wavevector q. Representative SEM images of (B) the 6nPEG gel network prior to mineralization (Scale bar = 1 μm) and (C) the fully mineralized gel, with the latter revealing a uniform dispersion of Fe_3O_4 (larger crystal particles in the image) and $Fe(OH)_2$ (bright hairlike whiskers in the image) (Scale bar = 1 μm). Representative TEM images of the resin-embedded mineralized gel sample with (D) smaller (Scale bar = 0.5 μm) and (E) larger Fe_3O_4 iron oxide particles (i.e., the particles that are visible in (C)) (Scale bar = 1 μm). (F) Diffraction patterns observed in the larger iron oxide particles (Scale bar = 20 nm). The inset shows a (112) diffraction pattern of Fe_3O_4 (Scale bar = 10 nm^{-1}).

mineralized gel as shown in Figure 3B. We hypothesize that the increased modulus of the mineralized gel is likely due to a nontrivial combination of factors, such as particle size heterogeneity, interphase formation around the iron oxide minerals,[39,40] and polymer incorporation inside grown iron oxide minerals.[41,42]

2.4. Structural Characterizations. We now pair the mechanical measurements of the mineralized gels with structural characterizations of the minerals in the gel. First, small-angle X-ray scattering (SAXS) experiments revealed a dramatic difference in the scattering intensity of the mineralized gel compared to an unmineralized gel, in support of formation of compounds with high electron contrast compared to the hydrogel constituents (polymer and water), as expected upon mineralization and consistent with prior work (Figure 4A).[21] Structural differences between the two gels are also obvious in scanning electron microscopy (SEM) images of the gels. The samples are prepared by glutaraldehyde fixation and a tetramethylsilane-based air-drying procedure that allows the hydrogels to retain microstructural features for imaging.[19,43,44] The mineralized gels show an abundance of large particles (Figure 4C) that are absent in the unmineralized gels (Figure 4B). Transmission electron microscopy (TEM) images of the gel specimens prepared as for SEM but embedded in resin and microtomed, reveal two regions of different particle sizes, where one region exhibits a mean diameter of $\langle D \rangle \approx 28$ nm (Figure 4D) and another region exhibits a mean diameter of $\langle D \rangle \approx 96$ nm (Figure 4E). The larger particles show obvious lattice fringes, consistent with the diffraction planes of Fe_3O_4 magnetite (Figure 4F). Energy-dispersive spectroscopy (EDS) analysis of the TEM samples confirms that the elemental composition of the observed

particles is dominated by Fe and O signals (Figure S1A−C). Since no extra effort was made to prevent the autoxidation of Fe_3O_4, some presence of iron hydroxides as well as a mixture of iron oxide phases is expected in the gel. Accordingly, we observed the presence of unreacted iron hydroxides, which take a whisker or plate-like form in SEM (Figure 4B) and TEM images (Figure S2).[29] Bulk XRD experiments reveal a coexistence of magnetite (Fe_3O_4) and hematite (Fe_2O_3) (Figure S3).

The presence of remnant nitrocatechol groups in the partially covalent 6nPEG network is critical for *in situ* mineralization of Fe_3O_4, as these groups can coordinate with grown iron oxide particles and stabilize them in the network due to the strong interactions with the iron ions on the particle surface.[18,35,45] In the absence of these sticky functional groups, we would expect that the polymer network is not able to retain Fe_3O_4 particles in the hydrogel matrix. To demonstrate this, we synthesized covalently cross-linked poly(acrylamide) hydrogels with the same elastic modulus of 1 kPa, swelled the gel, and performed the same *in situ* mineralization reaction. As expected, we observe that the iron oxide minerals are not retained inside the gel: upon preparing the sample for SEM imaging, we find an absence of magnetite particles in the microstructure of the gel (Figure 5A,B). We also observe significantly lower reinforcement from the mineralization process, as shown by rheological measurements (Figure 5C). This suggests that the *in situ* mineralization reaction described here necessitates a strong iron oxide binding ligand to stabilize the grown particles in the network.

2.5. Functional Magnetic Hydrogels. Finally, we leveraged these insights to design a functional hydrogel material at the bulk scale with magneto-responsive properties
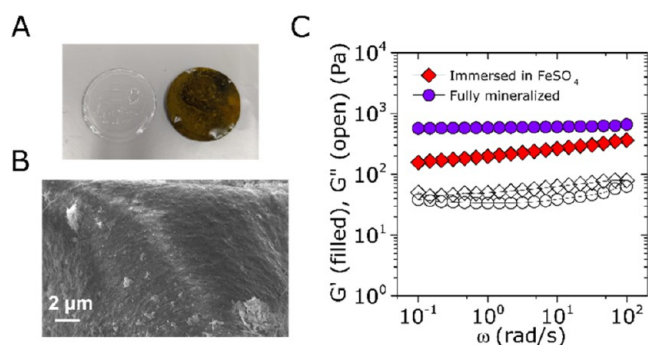
Figure 5. Mineralization in poly(acrylamide) hydrogels without metal-coordinate chemistry. (A) Images of the swollen poly-(acrylamide) hydrogels before and after mineralization. (B) Representative SEM micrographs of the mineralized poly(acrylamide) hydrogels. The mineralized poly(acrylamide) samples do not exhibit the iron oxide particles shown in the mineralized 6nPEG sample (Figure 4C), and instead, they show features more reminiscent of the mineral-free 6nPEG sample (Figure 4B) (Scale bar = 2 μm). (C) Rheological characterization of the poly(acrylamide) hydrogels before and after mineralization, showing only a two-fold increase in G' at $\omega =$ 100 rad/s.

that arise from Fe_3O_4. To do so, we first characterized the saturation magnetization of the fully mineralized system using a Superconducting Quantum Interference Device (SQUID). The mineralized gel reaches a saturation magnetization M_{sat} ~4.5 emu/g at a magnetic field of 70,000 Oe (Figure 6A). The M_{sat} value is more than two times larger than that reported in our prior study, where Fe_3O_4 was mineralized via coprecipitation in a catechol network over five repeated cycles. Nevertheless, this value remains considerably smaller than that of bulk Fe_3O_4 reported to be M_{sat} ~86 emu/g,[46] which can be explained by the size-dependence of M_{sat}[47,48] as well as the presence of other amorphous or poorly crystalline components in the network.

To make a bulk-scale gel strip, it is necessary to slow the rapid oxidation reaction between nitrocatechol and $NaIO_4$ to encourage full mixing of the reagents. We achieve this by first mixing $NaIO_4$ with HCl, adding this mixture to the polymer solution and finally raising the pH by adding NaOH (equal parts with HCl) and NaAc buffer. This results in a slow activation of $NaIO_4$ and thus a slowing down of the oxidative cross-linking of nitrocatechol. Overnight curing of 6nPEG in this manner results in a homogenous, partially covalent gel

(Figure 6B). When these gel strips are mineralized (Figure 6C), we find that the resulting nanocomposite hydrogels exhibit significant actuation ability, as evidenced by the reversible actuation of the fully hydrated strip with commercial N52 neodymium magnets (Figure 6D and Movie 1).

Overall, our soft viscoelastic magnetic hydrogel system demonstrates several material properties that facilitate applications in clinically relevant areas such as drug delivery, magnetic endoscopy, and soft robotics. In this vein, future work would be important to assess how factors such as the size and concentration of the grown iron oxide minerals, the density of metal-coordinating ligands in the hydrogels, and the mesh size of the hydrogels affect particle retention and magnetic actuation ability. Similarly, a more systematic characterization of the mechanical properties of the mineralized hydrogels that would enable these applications such as tensile strength, fracture toughness, and fatigue—which would now be possible with the bulk-scale gel strips synthesized in Figure 6B,C—would be a natural extension of the study.

3. CONCLUSIONS

We have demonstrated that partially covalent nitrocatechol-functionalized polymer networks can serve as scaffolds for high-yield bath-scale mineralization of iron oxides. This process results in the formation of mineralized hydrogels with a high concentration (57 wt % dry mass) of large iron oxide particles (~100 nm in diameter), which are strongly coupled to the polymer network, thus resulting in the formation of a mechanically reinforced viscoelastic and magneto-responsive material. In conjunction with our prior work,[21] these results highlight the ability of catechol-based groups to facilitate matrix stabilization of magnetic particles in hydrogels in a manner decoupled from mesh size control via polymer densification. Looking ahead, we anticipate that these approaches can be generalized and extended to accommodate other metal—ligand combinations with strong complexation ability and functional properties arising from the oxide minerals, for instance, catechol-titanium and imidazole-zinc to form composite materials with photocatalytic oxides.

4. METHODS

4.1. Materials and Methods. *4.1.1. Synthesis. 4.1.1.1. Polymer Synthesis.* 6-Arm PEG *N*-Hydrosuccinimide (15 kDa) was purchased from JenKem Technology. All other chemicals were purchased from Sigma-Aldrich and used without modifications. The 6nPEG polymers
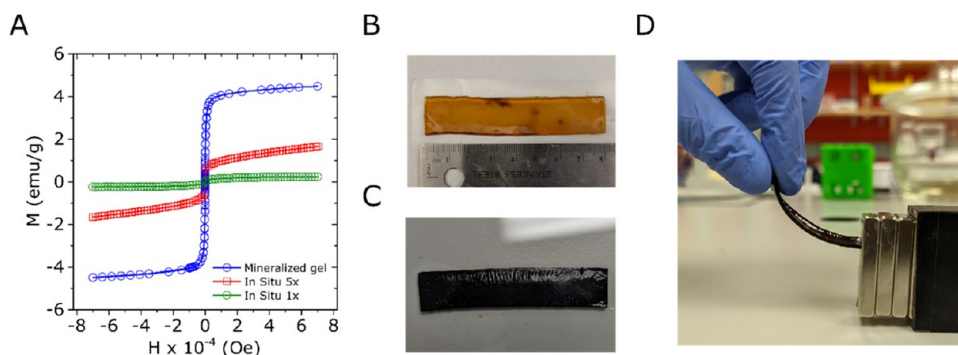
Figure 6. Magnetic actuation of the mineralized hydrogels. (A) SQUID characterization of the fully mineralized sample. The magnetization data are compared to those from our prior study using dropwise coprecipitation (1 cycle and 5 cycles).[21] (B) Image of a swollen bulk-scale 6nPEG hydrogel strip. (C) Image of the hydrogel strip after mineralization. (D) Magnetic actuation of the hydrogel strip from a N52 neodymium magnet (see Movie 1).

were made in an identical manner to the procedure described in ref 19.

4.1.1.2. Partially Covalent Gel Synthesis. Partially covalent 6nPEG networks were synthesized by mixing equal volumes of 6nPEG solution (200 mg/mL) and $NaIO_4$ in the cap of a 1 dram Kimble vial, where the concentration of $NaIO_4$ is varied to satisfy the ligand-to-$NaIO_4$ ratios illustrated in Figure 1C. The reaction results in gelation of the system within seconds. The reaction is allowed to proceed for 3 h, after which the gel is carefully extracted from the 1 dram vial cap with a knife. The gel is then swollen overnight in excess water to remove excess $NaIO_4$.

To make a bulk-scale strip of the partially covalent gel, 200 μL of 6nPEG solution (350 mg/mL) is mixed with 350 μL of $NaIO_4$–HCl mixture (0.036 M $NaIO_4$, 0.4 M HCl), which is then neutralized with the addition of 140 μL of NaOH (1.0 M) followed by 50 μL of NaAc buffer (3.0 M). This slower-gelling mixture is poured into the desired mold and allowed to gel for at least 6 h. The gel is then swollen overnight in excess water to remove excess $NaIO_4$.

4.1.1.3. Mineralized Gel Synthesis. The mineralization reaction is performed in the partially covalent 6nPEG following the method reported on prior study in gelatin,[28] with modifications. The swollen partially covalent crosslinked gel is extracted from the excess water and placed in a Petri dish. 1 mL of $FeSO_4$ (1 M) is added to the gel and allowed to absorb into the network for 3 h. A 10 mL solution of KNO_3 (1.0 M) and KOH (0.2 M) is then added to the gel and $FeSO_4$ mixture. The resulting solution is initially green and gradually becomes black. This reaction is allowed to proceed overnight. The final gel sample is swollen in excess water for 2 h to remove excess ions in the gel and used for further characterization.

4.1.1.4. Polyacrylamide Gel Synthesis. Polyacrylamide hydrogels were synthesized by making a 10 mL mixture of acrylamide (20 wt %), bis-acrylamide (0.2 wt %), and ammonium persulfate (5.0 wt %) at a volumetric ratio of 100:30:1. Cross-linking was activated with the addition of 5 μL TEMED.

4.1.2. Characterization. 4.1.2.1. Linear Rheology. All rheological characterizations were performed on an Anton Paar MCR-302 stress-controlled rheometer using a 10 mm parallel plate. All gels were loaded, trimmed, and sealed with mineral oil prior to characterization to prevent dehydration. Oscillatory shear strain experiments (strain amplitude γ_0 = 1%) were conducted over a range of frequencies to obtain the storage modulus $G'(\omega)$ and the loss modulus $G''(\omega)$.

4.1.2.2. Thermal Gravimetric Analysis (TGA). The composition of the mineralized gels was characterized by using a TA Discovery TGA with high-temperature platinum pans. Mass measurements were performed by performing equilibration at 25 °C, after which the oven temperature was ramped up to 550 °C at 10 °C/min under nitrogen gas flow-rates of 25 mL/min. The wt % of inorganics within the sample in a wet state was characterized by taking the mass ratio at 550 and 25 °C; the wt % of inorganics in the sample in a dry state was characterized by taking the mass ratio at 550 and 250 °C.

4.1.2.3. Scanning Electron Microscopy (SEM). All SEM images were obtained using a Zeiss Crossbeam 540 field-emission SEM operating on a secondary electron scattering mode at 5 kV with currents of 150 pA. Samples were prepared by first introducing them into a chemical fixative of 2% glutaraldehyde, after which the samples were gradually dehydrated in ethanol of increasing concentrations (35, 45, 55, 65, 75, 85, 95, and 100%). The samples were then introduced into ethanol:tetramethylsilane mixtures with increasing concentrations of tetramethylsilane (50, 80, 100 of tetramethylsilane, rest ethanol) and air-dried under the fume hood. This drying procedure results in some affine shrinkage in the hydrogel but allows the hydrogels to retain salient microstructural features for imaging.[19,43,44]

4.1.2.4. Transmission Electron Microscopy (TEM). All TEM images of the gels were obtained using a JEOL 2100 FEG microscope using the biggest area size of a parallel illumination beam and a 100 μm diameter condenser aperture and operating at 200 kV. All images were recorded on a Gatan 2k × 2k UltraScan CCD camera. STEM imaging was done using a HAADF (high-angle annular dark field) detector with a 0.5 nm probe size and 12 cm camera length. X-Max 80

mm^2 EDX (Oxford Instrument, U.K.) was used for obtaining energy-dispersive X-ray spectroscopy (EDS) of the samples.

Images of the iron oxide particles formed in a dilute solution were obtained using an FEI Tecnai G2 Spirit Twin TEM. The samples were prepared by adding 0.1 mL of $FeSO_4$ (0.1 M) to a 10 mL mixture of KOH (0.2 M) and KNO_3 (1.0 M). The resulting solution was diluted to 1/1000th of the original concentration and dropped onto a 200 mesh carbon-coated copper holey grid from Ted-Pella and air-dried.

4.1.2.5. Small-Angle X-ray Scattering (SAXS). SAXS experiments were performed with a Bruker Nanostar SAXS instrument with a Pilatus3R 300 K detector. All samples were prepared by placing a thin gel sample inside a flat washer and sandwiching the washer with 5−7 μm thick mica sheets from SAXSLAB. The mica sheets are glued on the rim of the washer on both sides by using a Torr seal (carefully done to avoid sample contamination with Torr). A 2 mm beamstop with a sample-to-detector distance of 1509.1 mm was used to measure the SAXS response of the samples, with an exposure time of 1200 s. Obtained SAXS intensities were subtracted by a blank washer sandwiched by mica sheets.

4.1.2.6. X-ray Diffraction (XRD). XRD experiments were performed by using a Bruker D8 GADDS diffractometer using a Co radiation source to mitigate fluorescence from Fe samples, which would normally occur with a Cu radiation source. The hydrogels were dehydrated prior to measurement . Diffraction data were collected over a 2θ range of 15−80° at 40 kV and 40 mA, and resulting peaks were identified on HighScore Plus.

4.1.2.7. Superconducting Quantum Interference Device (SQUID) Magnetometry. All SQUID experiments were performed on dry hydrogels. For a given sample, the mass of the sample was recorded and the sample was then heat-sealed in a small cut piece of polypropylene straw. The sealed piece of straw was then pushed into the center of another straw and loaded to the SQUID device. All measurements were conducted using DC measurement modes at 300 K, and magnetic moments were characterized by alternating the magnetic field across ±70,000 Oe.

■ ASSOCIATED CONTENT

⑤ Supporting Information

The Supporting Information is available free of charge at https://pubs.acs.org/doi/10.1021/acsami.3c08145.

> Additional TEM, EDS, and XRD characterization of the mineralized hydrogel (PDF)

> Magnetic actuation of the mineralized hydrogel strip from N52 neodymium magnets (MP4)

■ AUTHOR INFORMATION

Corresponding Authors

Gareth H. McKinley — Department of Mechanical Engineering, Massachusetts Institute of Technology, Cambridge, Massachusetts 02139, United States; ⑩ orcid.org/0000-0001-8323-2779; Email: gareth@mit.edu

Niels Holten-Andersen — Department of Bioengineering and Materials Science and Engineering, Lehigh University, Bethlehem, Pennsylvania 18015, United States; ⑩ orcid.org/0000-0002-5318-9674; Email: nih221@lehigh.edu

Authors

Jake Song — Department of Materials Science and Engineering, Massachusetts Institute of Technology, Cambridge, Massachusetts 02139, United States; Present Address: Department of Mechanical Engineering, Stanford University, Stanford, California 94305, United States; ⑩ orcid.org/0000-0003-1254-6206

Sungjin Kim − *Department of Materials Science and Engineering, Massachusetts Institute of Technology, Cambridge, Massachusetts 02139, United States;* Present Address: Department of Chemical and Biological Engineering, University of New Mexico, Albuquerque, New Mexico 87131, United States; ● orcid.org/0000-0002-2068-9189

Olivia Saouaf − *Department of Materials Science and Engineering, Massachusetts Institute of Technology, Cambridge, Massachusetts 02139, United States;* Present Address: Department of Materials Science and Engineering, Stanford University, Stanford, California 94305, United States

Crystal Owens − *Department of Mechanical Engineering, Massachusetts Institute of Technology, Cambridge, Massachusetts 02139, United States;* Present Address: Computer Science and Artificial Intelligence Laboratory, Massachusetts Institute of Technology, Cambridge, Massachusetts 02139, United States; ● orcid.org/0000-0002-2433-7025

Complete contact information is available at:
https://pubs.acs.org/10.1021/acsami.3c08145

Notes
The authors declare no competing financial interest.

■ REFERENCES

(1) Ze, Q.; Kuang, X.; Wu, S.; Wong, J.; Montgomery, S. M.; Zhang, R.; Kovitz, J. M.; Yang, F.; Qi, H. J.; Zhao, R. Magnetic Shape Memory Polymers with Integrated Multifunctional Shape Manipulation. *Adv. Mater.* **2020**, *32* (4), No. 1906657.

(2) Zhu, W.; Li, J.; Leong, Y. J.; Rozen, I.; Qu, X.; Dong, R.; Wu, Z.; Gao, W.; Chung, P. H.; Wang, J.; Chen, S. 3d-Printed Artificial Microfish. *Adv. Mater.* **2015**, *27* (30), 4411−4417.

(3) Cai, L.; Xu, D.; Chen, H.; Wang, L.; Zhao, Y. Designing Bioactive Micro-/Nanomotors for Engineered Regeneration. *Eng. Regener.* **2021**, *2*, 109−115.

(4) Kim, Y.; Parada, G. A.; Liu, S.; Zhao, X. Ferromagnetic Soft Continuum Robots. *Sci. Rob.* **2019**, *4* (33), No. eaax7329.

(5) Wu, S.; Hu, W.; Ze, Q.; Sitti, M.; Zhao, R. Multifunctional Magnetic Soft Composites: A Review. *Multifunct. Mater.* **2020**, *3* (4), No. 042003.

(6) Cox, T. R.; Erler, J. T. Remodeling and Homeostasis of the Extracellular Matrix: Implications for Fibrotic Diseases and Cancer. *Dis. Models Mech.* **2011**, *4* (2), 165−178.

(7) Rahmati, M.; Silva, E. A.; Reseland, J. E.; Heyward, C. A.; Haugen, H. J. Biological Responses to Physicochemical Properties of Biomaterial Surface. *Chem. Soc. Rev.* **2020**, *49* (15), 5178−5224.

(8) Chaudhuri, O.; Cooper-White, J.; Janmey, P. A.; Mooney, D. J.; Shenoy, V. B. Effects of Extracellular Matrix Viscoelasticity on Cellular Behaviour. *Nature* **2020**, *584* (7822), 535−546.

(9) Tringides, C. M.; Vachicouras, N.; de Lázaro, I.; Wang, H.; Trouillet, A.; Seo, B. R.; Elosegui-Artola, A.; Fallegger, F.; Shin, Y.; Casiraghi, C.; et al. Viscoelastic Surface Electrode Arrays to Interface with Viscoelastic Tissues. *Nat. Nanotechnol.* **2021**, *16* (9), 1019−1029.

(10) Messing, R.; Frickel, N.; Belkoura, L.; Strey, R.; Rahn, H.; Odenbach, S.; Schmidt, A. M. Cobalt Ferrite Nanoparticles as Multifunctional Cross-Linkers in PAAM Ferrohydrogels. *Macromolecules* **2011**, *44* (8), 2990−2999.

(11) Li, Y.; Huang, G.; Zhang, X.; Li, B.; Chen, Y.; Lu, T.; Lu, T. J.; Xu, F. Magnetic Hydrogels and Their Potential Biomedical Applications. *Adv. Funct. Mater.* **2013**, *23* (6), 660−672.

(12) Helminger, M.; Wu, B.; Kollmann, T.; Benke, D.; Schwahn, D.; Pipich, V.; Faivre, D.; Zahn, D.; Cölfen, H. Synthesis and Characterization of Gelatin-Based Magnetic Hydrogels. *Adv. Funct. Mater.* **2014**, *24* (21), 3187−3196.

(13) Shi, X.; Shi, Z.; Wang, D.; Ullah, M. W.; Yang, G. Microbial Cells with a Fe_3O_4 Doped Hydrogel Extracellular Matrix: Manipulation of Living Cells by Magnetic Stimulus. *Macromol. Biosci.* **2016**, *16* (10), 1506−1514.

(14) Zhang, Y.; Yang, B.; Zhang, X.; Xu, L.; Tao, L.; Li, S.; Wei, Y. A Magnetic Self-Healing Hydrogel. *Chem. Commun.* **2012**, *48* (74), 9305−9307.

(15) Waite, J. H.; Andersen, N. H.; Jewhurst, S.; Sun, C. Mussel Adhesion: Finding the Tricks Worth Mimicking. *J. Adhes.* **2005**, *81* (3−4), 297−317.

(16) Holten-Andersen, N.; Waite, J. Mussel-Designed Protective Coatings for Compliant Substrates. *J. Dent. Res.* **2008**, *87* (8), 701−709.

(17) Lee, H.; Scherer, N. F.; Messersmith, P. B. Single-Molecule Mechanics of Mussel Adhesion. *Proc. Natl. Acad. Sci. U.S.A.* **2006**, *103* (35), 12999−13003.

(18) Li, Q.; Barrett, D. G.; Messersmith, P. B.; Holten-Andersen, N. Controlling Hydrogel Mechanics Via Bio-Inspired Polymer−Nanoparticle Bond Dynamics. *ACS Nano* **2016**, *10* (1), 1317−1324.

(19) Song, J.; Rizvi, M. H.; Lynch, B. B.; Ilavsky, J.; Mankus, D.; Tracy, J. B.; McKinley, G. H.; Holten-Andersen, N. Programmable Anisotropy and Percolation in Supramolecular Patchy Particle Gels. *ACS Nano* **2020**, *14* (12), 17018−17027.

(20) Song, J.; Zhang, Q.; de Quesada, F.; Rizvi, M. H.; Tracy, J. B.; Ilavsky, J.; Narayanan, S.; Del Gado, E.; Leheny, R. L.; Holten-Andersen, N.; McKinley, G. H. Microscopic Dynamics Underlying the Stress Relaxation of Arrested Soft Materials. *Proc. Natl. Acad. Sci. U.S.A.* **2022**, *119* (30), No. e2201566119.

(21) Kim, S.; Regitsky, A. U.; Song, J.; Ilavsky, J.; McKinley, G. H.; Holten-Andersen, N. In Situ Mechanical Reinforcement of Polymer Hydrogels Via Metal-Coordinated Crosslink Mineralization. *Nat. Commun.* **2021**, *12* (1), No. 667.

(22) Menyo, M. S.; Hawker, C. J.; Waite, J. H. Versatile Tuning of Supramolecular Hydrogels through Metal Complexation of Oxidation-Resistant Catechol-Inspired Ligands. *Soft Matter* **2013**, *9* (43), 10314−10323.

(23) Cencer, M.; Murley, M.; Liu, Y.; Lee, B. P. Effect of Nitro-Functionalization on the Cross-Linking and Bioadhesion of Biomimetic Adhesive Moiety. *Biomacromolecules* **2015**, *16* (1), 404−410.

(24) Baumgartner, J.; Dey, A.; Bomans, P. H.; Le Coadou, C.; Fratzl, P.; Sommerdijk, N. A. J. M.; Faivre, D. Nucleation and Growth of Magnetite from Solution. *Nat. Mater.* **2013**, *12* (4), 310−314.

(25) Sugimoto, T.; Matijević, E. Formation of Uniform Spherical Magnetite Particles by Crystallization from Ferrous Hydroxide Gels. *J. Colloid Interface Sci.* **1980**, *74* (1), 227−243.

(26) Vereda, F.; de Vicente, J.; del Puerto Morales, M.; Rull, F.; Hidalgo-Álvarez, R. Synthesis and Characterization of Single-Domain Monocrystalline Magnetite Particles by Oxidative Aging of $Fe(OH)_2$. *J. Phys. Chem. C* **2008**, *112* (15), 5843−5849.

(27) Mirabello, G.; Lenders, J. J.; Sommerdijk, N. A. Bioinspired Synthesis of Magnetite Nanoparticles. *Chem. Soc. Rev.* **2016**, *45* (18), 5085−5106.

(28) Sturm, S.; Siglreitmeier, M.; Wolf, D.; Vogel, K.; Gratz, M.; Faivre, D.; Lubk, A.; Büchner, B.; Sturm, E. V.; Cölfen, H. Magnetic Nanoparticle Chains in Gelatin Ferrogels: Bioinspiration from Magnetotactic Bacteria. *Adv. Funct. Mater.* **2019**, *29* (45), No. 1905996.

(29) Altan, C. L.; Lenders, J. J.; Bomans, P. H.; de With, G.; Friedrich, H.; Bucak, S.; Sommerdijk, N. A. Partial Oxidation as a Rational Approach to Kinetic Control in Bioinspired Magnetite Synthesis. *Chem. - Eur. J.* **2015**, *21* (16), 6150−6156.

(30) Cazzell, S. A.; Holten-Andersen, N. Expanding the Stoichiometric Window for Metal Cross-Linked Gel Assembly Using Competition. *Proc. Natl. Acad. Sci. U.S.A.* **2019**, *116* (43), 21369−21374.

(31) Budday, S.; Ovaert, T. C.; Holzapfel, G. A.; Steinmann, P.; Kuhl, E. Fifty Shades of Brain: A Review on the Mechanical Testing and Modeling of Brain Tissue. *Arch. Comput. Methods Eng.* **2020**, *27* (4), 1187−1230.

(32) Handorf, A. M.; Zhou, Y.; Halanski, M. A.; Li, W.-J. Tissue Stiffness Dictates Development, Homeostasis, and Disease Progression. *Organogenesis* **2015**, *11* (1), 1−15.

(33) Roy, H. L.; Song, J.; McKinley, G. H.; Holten-Andersen, N.; Lenz, M. Valence Can Control the Non-Exponential Viscoelastic Relaxation of Reversible Multivalent Gels. 2021, arXiv:2112.07454. arXiv.org e-Print archive. https://arxiv.org/abs/2112.07454.

(34) Song, J.; Li, Q.; Chen, P.; Keshavarz, B.; Chapman, B. S.; Tracy, J. B.; McKinley, G. H.; Holten-Andersen, N. Dynamics of Dual-Junction-Functionality Associative Polymer Networks with Ion and Nanoparticle Metal-Coordinate Cross-Link Junctions. *J. Rheol.* **2022**, *66* (6), 1333−1345.

(35) Amstad, E.; Gehring, A. U.; Fischer, H.; Nagaiyanallur, V. V.; Hähner, G.; Textor, M.; Reimhult, E. Influence of Electronegative Substituents on the Binding Affinity of Catechol-Derived Anchors to Fe_3O_4 Nanoparticles. *J. Phys. Chem. C* **2011**, *115* (3), 683−691.

(36) Burla, F.; Tauber, J.; Dussi, S.; van Der Gucht, J.; Koenderink, G. H. Stress Management in Composite Biopolymer Networks. *Nat. Phys.* **2019**, *15* (6), 549−553.

(37) Rubinstein, M.; Colby, R. H. *Polymer Physics*; Oxford University Press, 2003; Vol. *23*, pp 263−315.

(38) Zhukhovitskiy, A. V.; Zhao, J.; Zhong, M.; Keeler, E. G.; Alt, E. A.; Teichen, P.; Griffin, R. G.; Hore, M. J. A.; Willard, A. P.; Johnson, J. A. Polymer Structure Dependent Hierarchy in Polymoc Gels. *Macromolecules* **2016**, *49* (18), 6896−6902.

(39) Deng, F.; Van Vliet, K. J. Prediction of Elastic Properties for Polymer−Particle Nanocomposites Exhibiting an Interphase. *Nanotechnology* **2011**, *22* (16), No. 165703.

(40) Martinez-Garcia, J. C.; Serraïma-Ferrer, A.; Lopeandía-Fernández, A.; Lattuada, M.; Sapkota, J.; Rodríguez-Viejo, J. A Generalized Approach for Evaluating the Mechanical Properties of Polymer Nanocomposites Reinforced with Spherical Fillers. *Nanomaterials* **2021**, *11* (4), No. 830.

(41) Lopez-Berganza, J. A.; Chen, S.; Espinosa-Marzal, R. M. Tailoring Calcite Growth through an Amorphous Precursor in a Hydrogel Environment. *Cryst. Growth Des.* **2019**, *19* (6), 3192−3205.

(42) Kim, Y.-Y.; Carloni, J. D.; Demarchi, B.; Sparks, D.; Reid, D. G.; Kunitake, M. E.; Tang, C. C.; Duer, M. J.; Freeman, C. L.; Pokroy, B.; et al. Tuning Hardness in Calcite by Incorporation of Amino Acids. *Nat. Mater.* **2016**, *15* (8), 903−910.

(43) Reville, W. J.; Heapes, M. M.; O'Sullivan, V. R. A Survey to Assess the Ultrastructural Preservation of Fixed Biological Samples after Air-Drying from Tetramethylsilane. *Microscopy* **1994**, *43* (2), 111−115.

(44) Dey, S.; Baul, T. B.; Roy, B.; Dey, D. A New Rapid Method of Air-Drying for Scanning Electron Microscopy Using Tetramethylsilane. *J. Microsc.* **1989**, *156* (2), 259−261.

(45) Amstad, E.; Gillich, T.; Bilecka, I.; Textor, M.; Reimhult, E. Ultrastable Iron Oxide Nanoparticle Colloidal Suspensions Using Dispersants with Catechol-Derived Anchor Groups. *Nano Lett.* **2009**, *9* (12), 4042−4048.

(46) Kemp, S. J.; Ferguson, R. M.; Khandhar, A. P.; Krishnan, K. M. Monodisperse Magnetite Nanoparticles with Nearly Ideal Saturation Magnetization. *RSC Adv.* **2016**, *6* (81), 77452−77464.

(47) Pei, W.; Kumada, H.; Natsume, T.; Saito, H.; Ishio, S. Study on Magnetite Nanoparticles Synthesized by Chemical Method. *J. Magn. Magn. Mater.* **2007**, *310* (2), 2375−2377.

(48) Goya, G. F.; Berquo, T. S.; Fonseca, F. C.; Morales, M. P. Static and Dynamic Magnetic Properties of Spherical Magnetite Nanoparticles. *J. Appl. Phys.* **2003**, *94* (5), 3520−3528.